OBSERVATIONS AND PRELIMINARY RESULTS ON THE SEISMIC SEQUENCE BETWEEN SANTORINI AND AMORGOS

Institute of Geodynamics, National Observatory of Athens

Networks – Installation of new instruments

The seismic activity in the area between Santorini and Amorgos is being recorded on a 24/7 basis from the Hellenic Unified Seismographic Network (HUSN). Particularly within the area of the sequence, the Institute of Geodynamics of the National Observatory of Athens (NOAIG) has improved the local seismicity monitoring by installing new seismological stations and by upgrading the existing ones in Amorgos (AMGA), Anafi (ANAF), Astypalaia (ASTA) and Santorini (Thirasia - SAP3 and Ancient Thira -THERA). These actions began in the island complex of Santorini as early as mid-January when the Institute for the Study and Monitoring of Santorini Volcano (ISMOSAV) announced a volcanic unrest in the caldera and were extended in February to the surrounding islands after the initiation of the seismic activity in the region of Anydros. Additionally, the seismological stations of the Aristotle University of Thessaloniki (AUTH) at Vourvoulos (THR2) and the Akrotiri lighthouse (THR9) were upgraded with digital instruments from NOAIG. The new stations that were installed in the area significantly contribute towards the more detailed monitoring of the activity and the more precise evaluation of the seismic parameters related to the sequence. New accelerometers were also installed at Amorgos (AMGA) and Astypalea (ASTA) replacing the old ones, whereas maintenance was carried out at THRA in Fira. The data from these stations are transmitted in real time to the center of operations of NOAIG and are also freely available to the HUSN and the international seismological research community. It is noteworthy that from 26/01/2025 up to 14/02/2025 a total of 46.64 TB (in/out) were transmitted to and from the NOAIG data center, eida.gein.noa.gr, with a maximum outward traffic of 1Gbits/sec, almost double the maximum traffic of recent years (**figure 1**). Also, on 07/03/2025, NOAIG in collaboration with the French University GeoAzur and the National Kapodistrian University of Athens (NKUA) carried out the installation of 7 ocean bottom seismographs-hydrophones in the seismically activated area.

At the same time, the activity is also being monitored by the permanent GNSS station THIR of the NOANET network of NOAIG at Pyrgos Kallistis, which was put into operation by the Institute’s staff on 12/02/2025. Additionally, on 12/02/2025, a new GNSS station was installed in Anydros isle by NOAIG in collaboration with the University of Patras and NKUA. The above two stations were put into operation in order to monitor the deformation in detail, in combination with data from pre-existing permanent GNSS continuous recording stations, which are installed in Imerovigli, Exo Gonia and Perissa.

The Hellenic National Tsunami Warning Centre (HL-NTWC) of NOAIG undertook the installation of a tide gauge (NOA-99, **figure 2**) in a small fishing shelter on the northeastern coast of Santorini. The choice of this specific location, which is located as close as possible to the focal area of the ongoing seismic activity, aims primarily at the timely recording and monitoring of sea level changes. With the addition of this station, the network of tide gauges implemented by HL-NTWC since 2013 is further expanded and currently numbers 16 stations. Additionally, informational material regarding the operation of NTWC, as well as general guidelines on self-protection measures against the risk of tsunami, have also been delivered to the authorities.

All the above stations are presented in **Figure 2.**

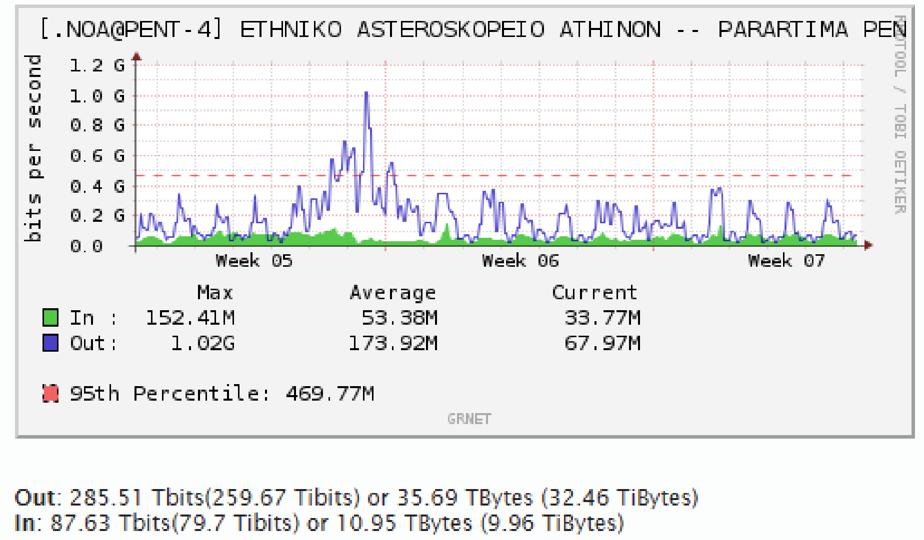

	Max	Average	Current
🟩 In :	152.41M	53.38M	33.77M
🟦 Out:	1.02G	173.92M	67.97M

🟥 95th Percentile: 469.77M

Out: 285.51 Tbits(259.67 Tibits) or 35.69 TBytes (32.46 TiBytes)
In: 87.63 Tbits(79.7 Tibits) or 10.95 TBytes (9.96 TiBytes)

Figure 1: Visualization of data transfer from the EIDA node for the period 26/01/2025 - 14/02/2025

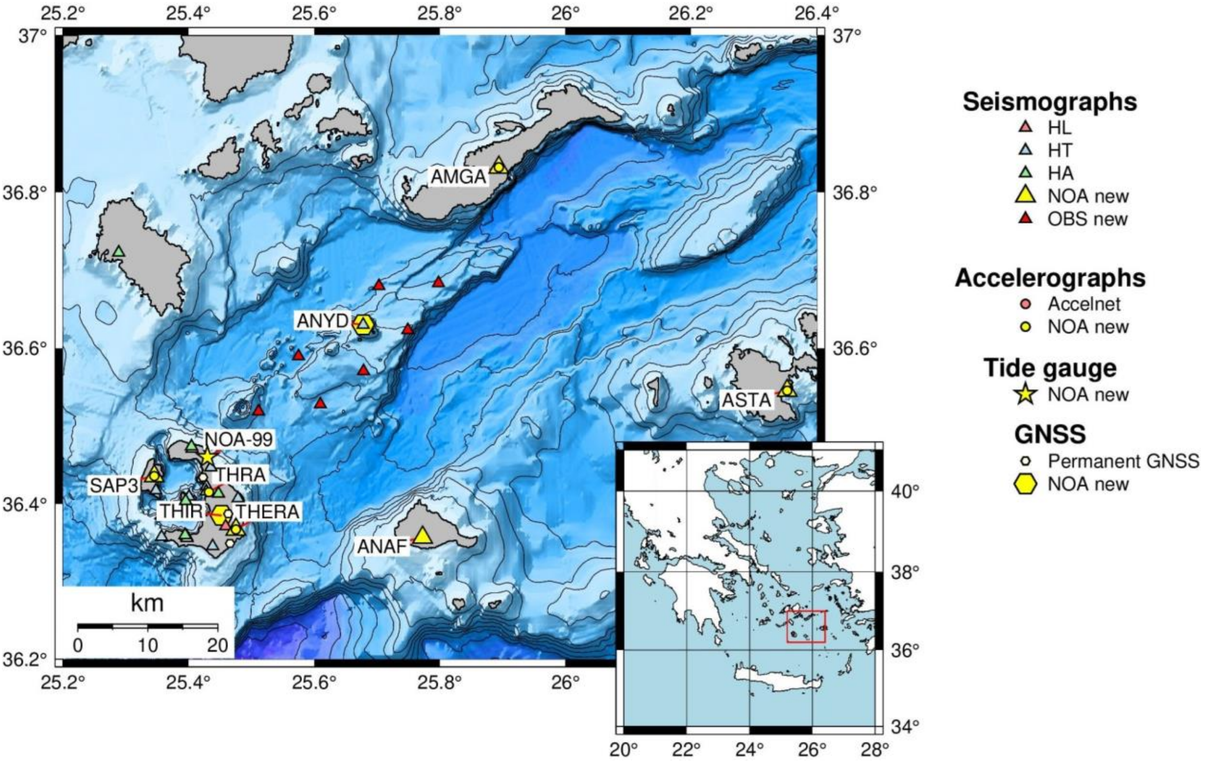

Figure 2: Stations (seismographs, accelerographs, GNSS and tide gauges) that are in operation in the broader region of the seismic activity. The new stations that have been installed by NOAIG are marked in the map.

Preliminary results

Seismicity monitoring

Seismic activity in the area between Santorini and Amorgos is monitored and analyzed on a 24/7 basis by the specialized staff of the NOAIG. During the period from 24/01/2025 to 06/03/2025 (23:59), a total of 4062 seismic events have been analyzed (**figures 3** and **4**), for which >154,000 P- and >62,000 S- first arrivals and >68,000 amplitude measurements have been obtained. In particular, from 02/02 onwards, more than 200 earthquakes have been analyzed daily (**figure 5a**). The majority of these earthquakes are recorded at depths between 7 and 15 km and in particular between 11 and 15 km (**figure 4b**). At the same time, the Institute provides the focal mechanisms for the most significant events of the sequence, which amount to 70 up to 06/03/2025 (23:59) and are presented in **figure 6**. These focal mechanisms have been automatically calculated by the Gisola software (Triantafylis et al., 2022), 10 of which have been re-evaluated by the Institute's staff.

Figure 5 shows the seismicity rate per day and the cumulative number of events for earthquakes with magnitudes (M) equal to or greater than M3.0, M3.5, M4.0 and M4.5. As of 06/03 (23:59), a total of 1407, 641, 226 and 61 earthquakes with magnitudes M3.0, M3.5, M4.0 and M4.5, respectively, have been recorded. The graph shows a significant increase in the seismicity rate on February 2, with 15 recorded earthquakes of magnitude ≥4, while in the following four days (February 3 – 6) the seismicity rate exceeded 25 earthquakes (M≥4) per day. On February 7, a decrease in the rate down to 8 seismic events (M≥4) is observed, which stabilizes in the following days at an average rate of 13 events (M≥4) per day. On February 12, an increase was observed, with 21 recorded earthquakes of magnitude M≥4, while on February 13, 2 earthquakes of magnitude M≥4 were recorded. Since then, and up until 19/02, a steady rate of earthquakes with magnitudes M≥4 has been observed, ranging from 2 to 5 events per day, whereas the last event with M≥4 was recorded on 24/02. Similarly, a decrease in the seismicity rate with magnitudes M≥3 and M≥3.5 was observed, with 19 and 7 events per day, respectively, from 13 to 20 February. Since then, a decrease in the seismicity rate is observed, with an average of 4 M≥3 per day.

Figure 7 shows the spatial distribution of seismicity in the Santorini-Amorgos zone during the period from January 25 to March 06, 2025, at 7-day intervals. Between January 24 and 31, some sporadic small-magnitude earthquakes occurred in the caldera of Santorini, with the largest being a magnitude M3.6 event southeast of Thirasia, while over on January 26-27 some sporadic small-magnitude earthquakes began to occur northeast of Santorini and the underwater Kolumbo volcano. Seismicity began to intensify in this area in the following days, between January 28 and 31, with seismic magnitudes not exceeding M3.2. This situation changed in the subsequent days with a rapid increase in the seismicity rate, with magnitudes greater than M3.0 and M4.0 (**Figure 5**), whereas a magnitude M5.0 earthquake was recorded on February 4. Seismicity during the period from February 1 to 4 showed a migration northeast of the area around the island of Anydros. High seismicity rates continued to be observed in the following days, with the largest event being a magnitude M5.2 earthquake on February 5. Seismicity during the period from February 1 to 7 was concentrated in the broader Anydros area. In the following period, between February 8 and 14, four earthquakes with magnitudes equal to or greater than M5.0 occurred, with the strongest being a magnitude M5.3 earthquake on February 10. Seismicity shifted northeast on February 11, before returning to the Anydros area in the following days. On February 17, a magnitude M5.1 earthquake occurred in the Anydros area, while on February 18, a magnitude 5.0 earthquake occurred, with the activation of the earthquake cluster to the east of Anydros. Since then, the seismicity has been concentrated in the broader Anydros region with smaller magnitude events.

The migration of seismicity is also evident in **Figure 8**, where the epicentral distance of the earthquakes is shown over time, relative to a point source defined as the average geographic location of the first 10 earthquakes in the sequence that occurred between January 26 and 27. It can be observed that while the average distance of the earthquakes remains constant over time between January 27 and 31, on February 1, a rapid migration of seismicity towards the northeast begins, with an average rate of approximately ~5 km per day. This migration was completed by February 5. Since then, seismicity has been shifting towards the southwest in the Anydros area up until February 9. On February 10 and 11, seismicity again shifted northeast, to the epicentral area of the magnitude M5.3 earthquake (**Figure 7**). After February 12, seismicity has been concentrated in the broader Anydros region without any significant migration.

The cumulative seismic moment with respect to time was also calculated since the start of the sequence (**figure 9**), based on the recorded seismic magnitudes (Kanamori & Heaton, 2000). The seismic moment is directly related to the energy released by an earthquake and is expressed in Newton•meter (Nm) in the graph. It is observed that the seismic moment increases with a steady rate from February 3, up to the early hours of February 6, after which it decreased over the following days until the evening of February 10, when the magnitude M5.3 and M5.0 earthquakes occurred. Since then, a relative decrease in the rate of increase of the cumulative seismic moment is observed. Some small increases that are observed are associated with larger earthquakes, such as the magnitude M5.0 earthquake on the 12th of February and the M5.1 and M5.0 earthquakes on February 17 and 18, respectively. After the 20th of February and the decrease of the earthquake magnitudes, the seismic moment remains relatively stable. It is also noted that the total seismic moment of the sequence has exceeded the corresponding seismic moment of a magnitude M6.0 earthquake and by February 20, it is equivalent to a M6.11 earthquake.

Finally, it is noted that intensity maps (USGS ShakeMap) are generated by the Institute in near real time and are available on the website: https://accelnet.gein.noa.gr/shakemaps/, which is open to the general public. An overview of the website and the results presents the maximum intensities calculated from instrumental measurements in the area, as well as all results from the automatic analysis of the accelerograms (**figures 10**-**12**).

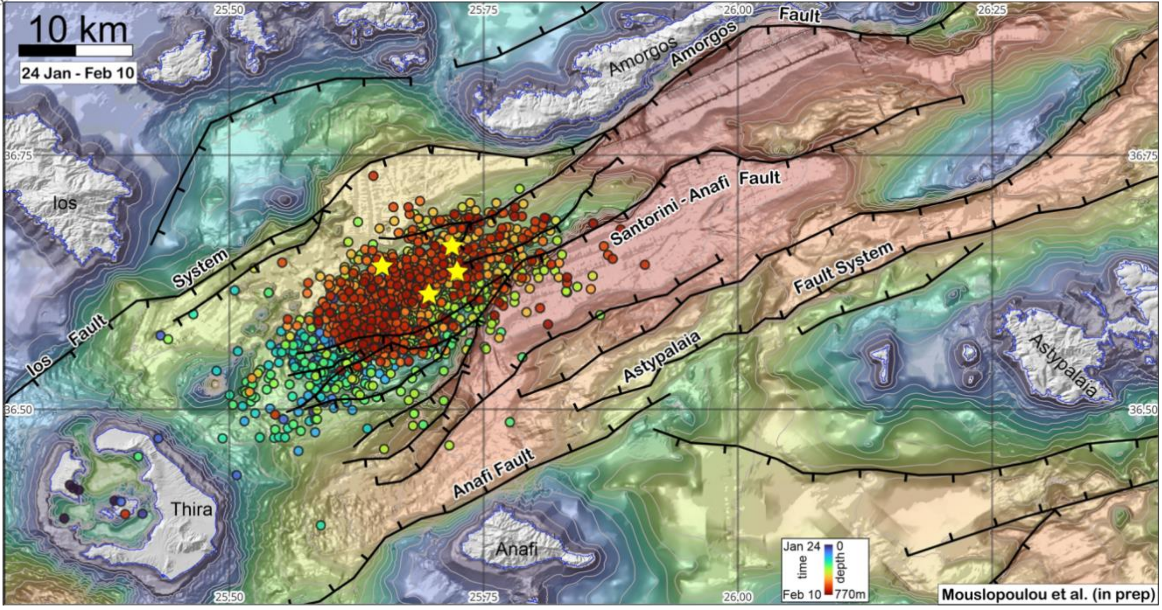

Figure 3: Digital relief map (https://emodnet.eu/bathymetry) depicting the main bathymetric structures of the Santorini – Amorgos tectonic depression. Black lines indicate active normal faults. Contours are at 50 m intervals. The seismic sequence covers the initial time period from 24/01/2025 to 10/02/2025 and is color-coded as a function of time (start: 24/01/2025). Stars indicate M≥5 earthquakes. The faults have been modified from Nomikou et al. (2018) and Andinisari et al. (2021). The presented seismicity is obtained by NOAIG.

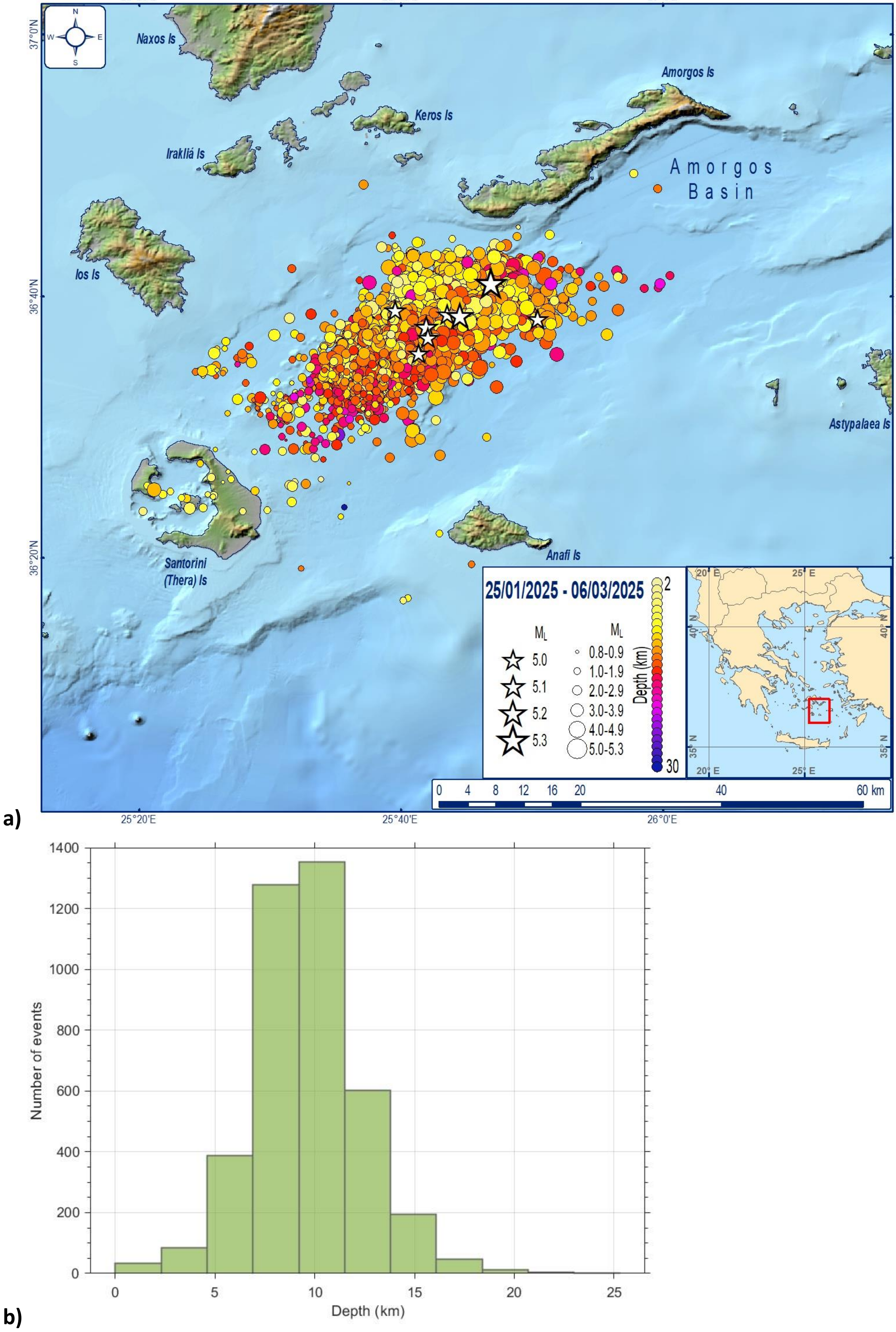

Figure 4: a) The seismic sequence recorded from 24/01/2025 up to 06/03/2025 in color scale related to the event depths, **b)** event depth distribution for the above events.

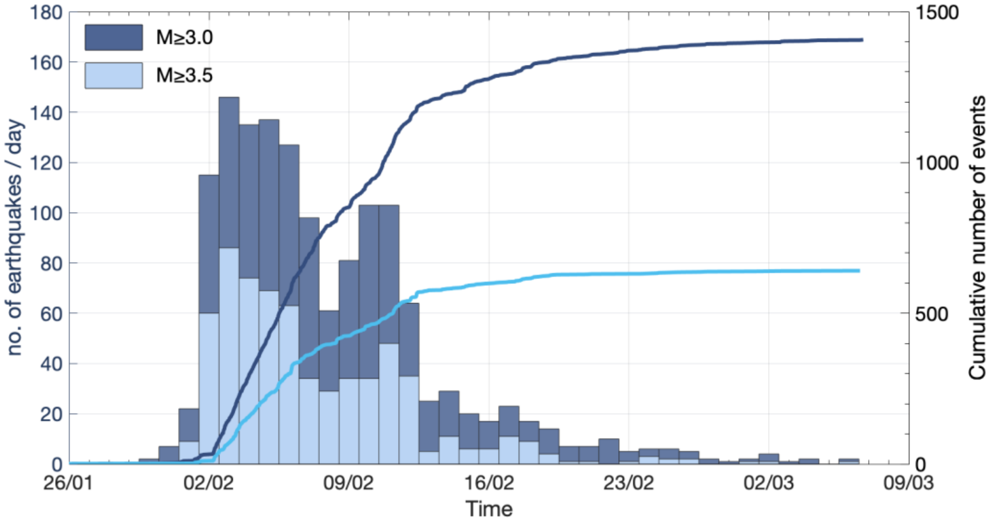

a)

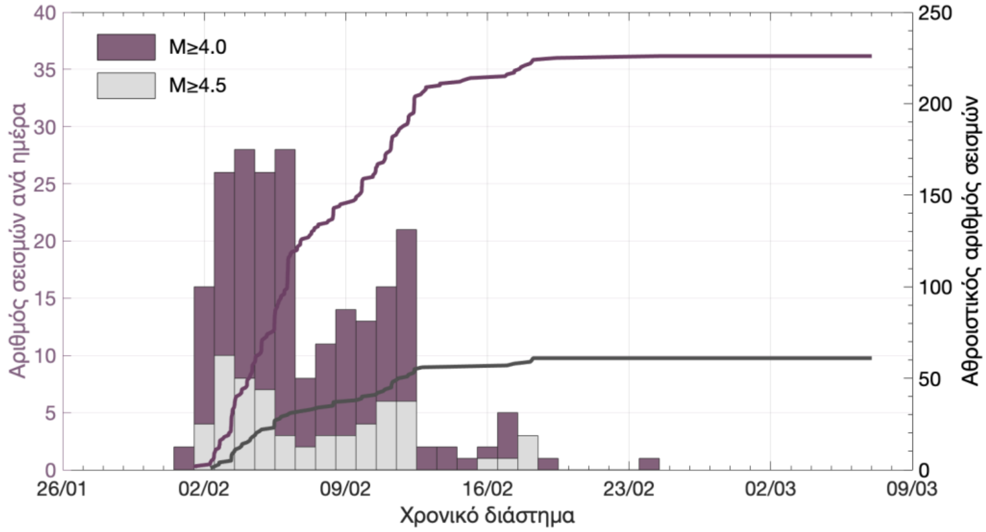

b)

Figure 5: a) Seismicity rate per day (histogram, left axis) and cumulative number of earthquakes (solid line, right axis), for magnitudes M≥3.0 and M≥3.5 and **b)** for magnitudes M≥4.0 and M≥4.5.

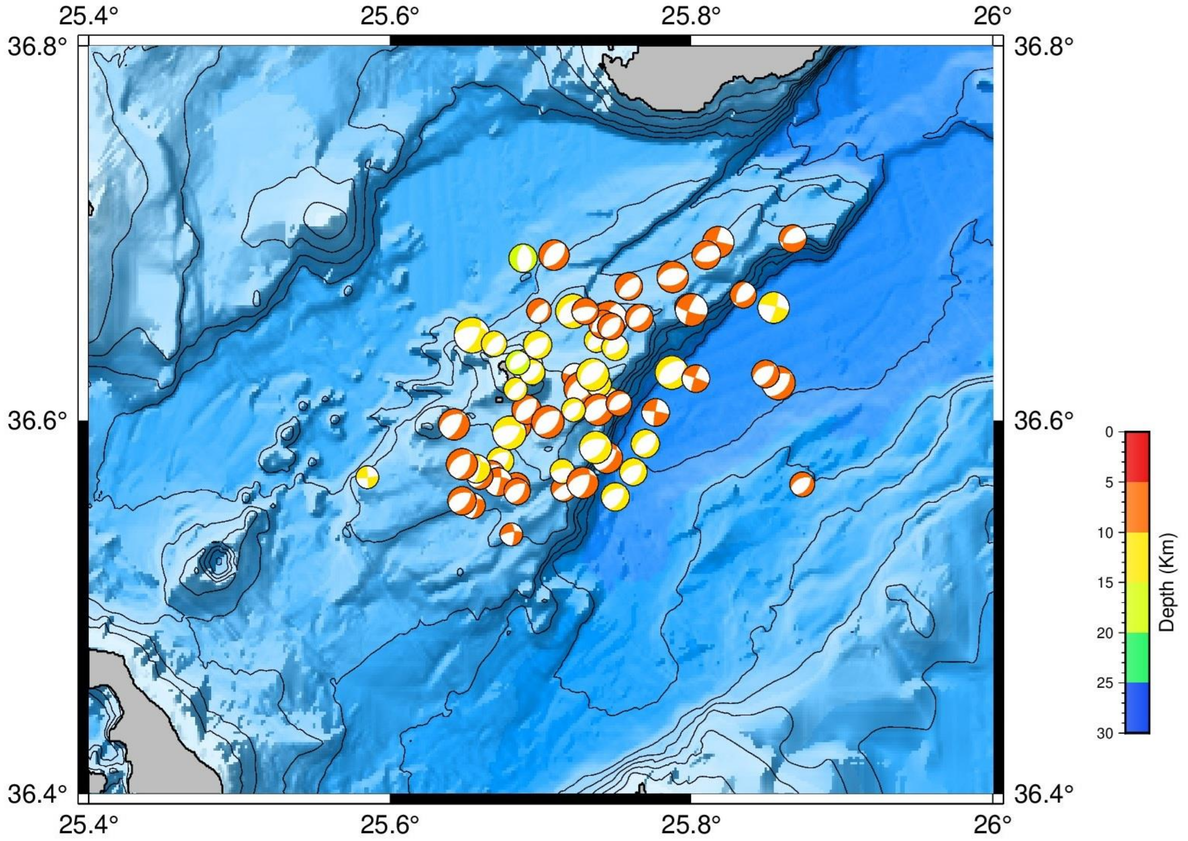

Figure 6: Calculated MT-solutions by NOAIG in the region.

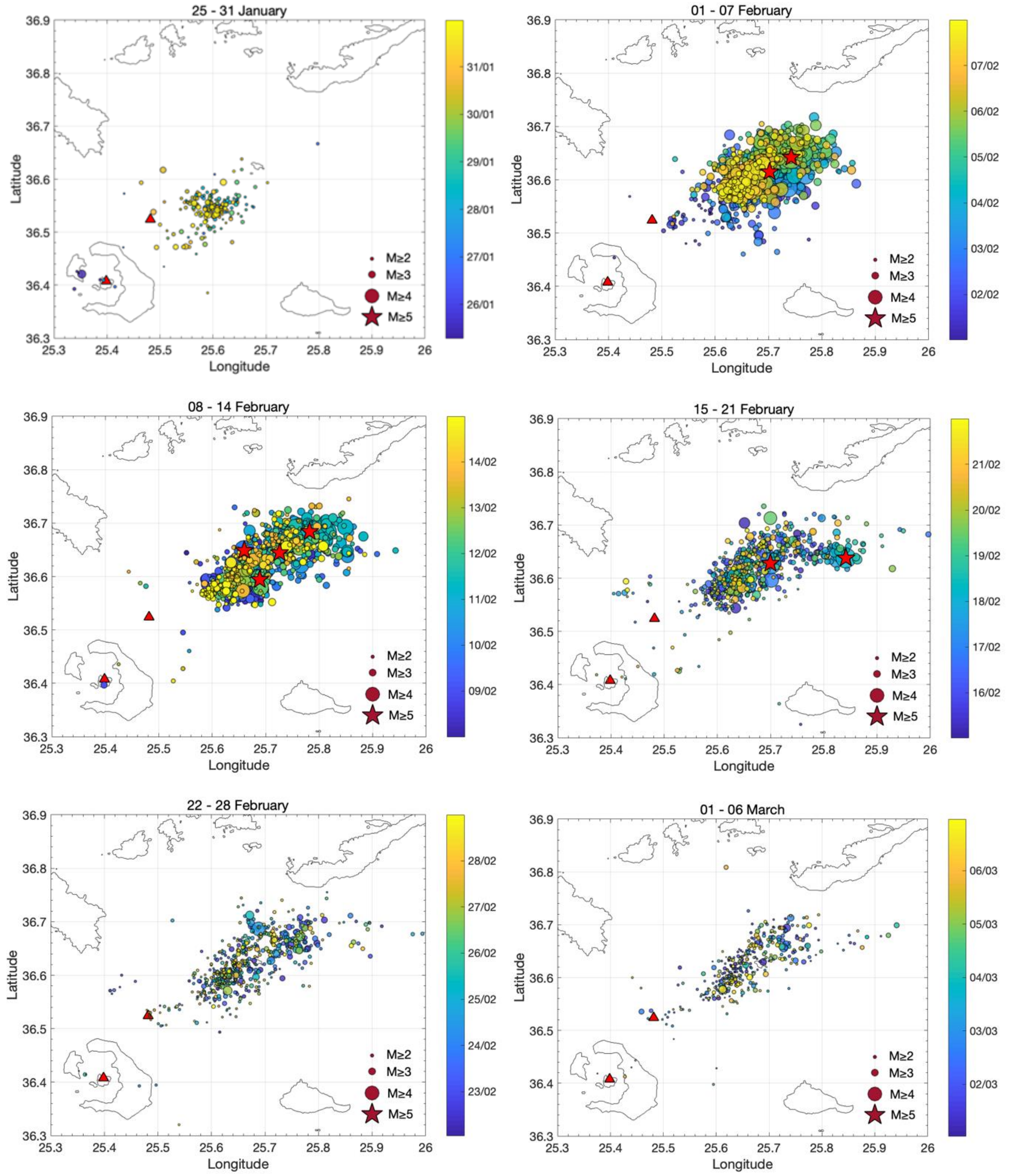

Figure 7: Seismicity maps for the Santorini – Amorgos region during the period between 25 January – 06 March 2025, distributed over 7-day intervals. The color scale is attributed to time and the symbol size is related to event magnitude. The triangles represent the volcanic centers of Nea Kameni and Kolumbo.

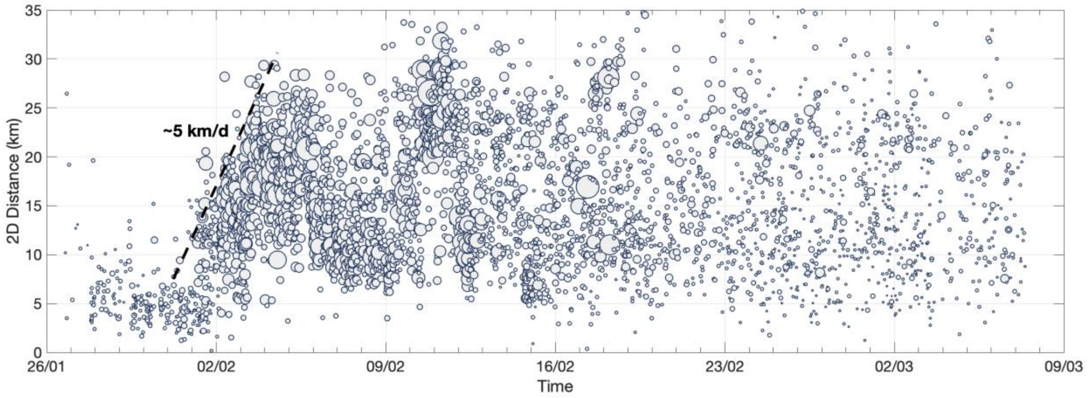

a)

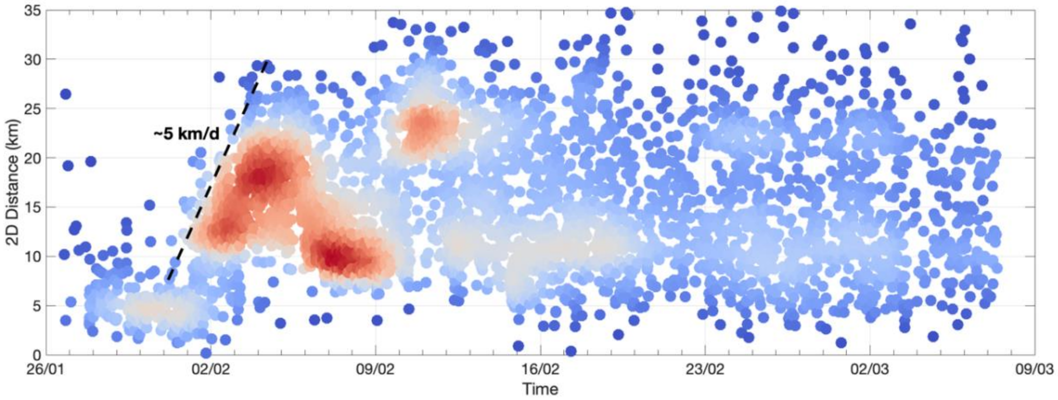

b)

Figure 8: **a)** Earthquake distance from a specific point source versus time with a symbol size relative to the event magnitude. **b)** Corresponding image with a colorscale relative to the event density. The dashed line indicates the migration rate of the earthquake epicenters.

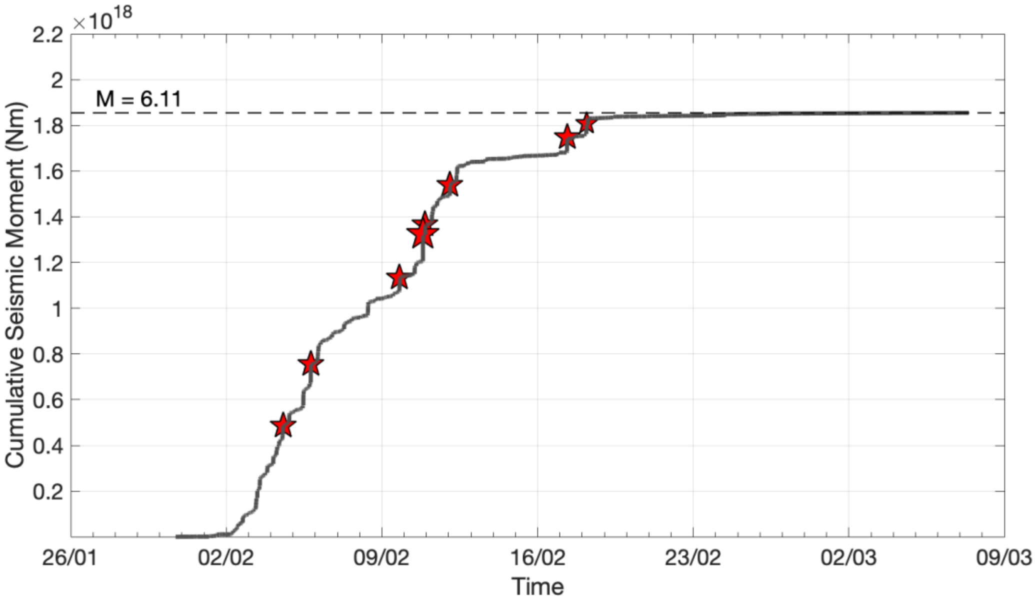

Figure 9: Cumulative seismic moment with respect to time. The symbols (stars) indicate earthquakes with magnitude M≥5.0, while the dashed line indicates the corresponding seismic moment of a magnitude M6.0 earthquake.

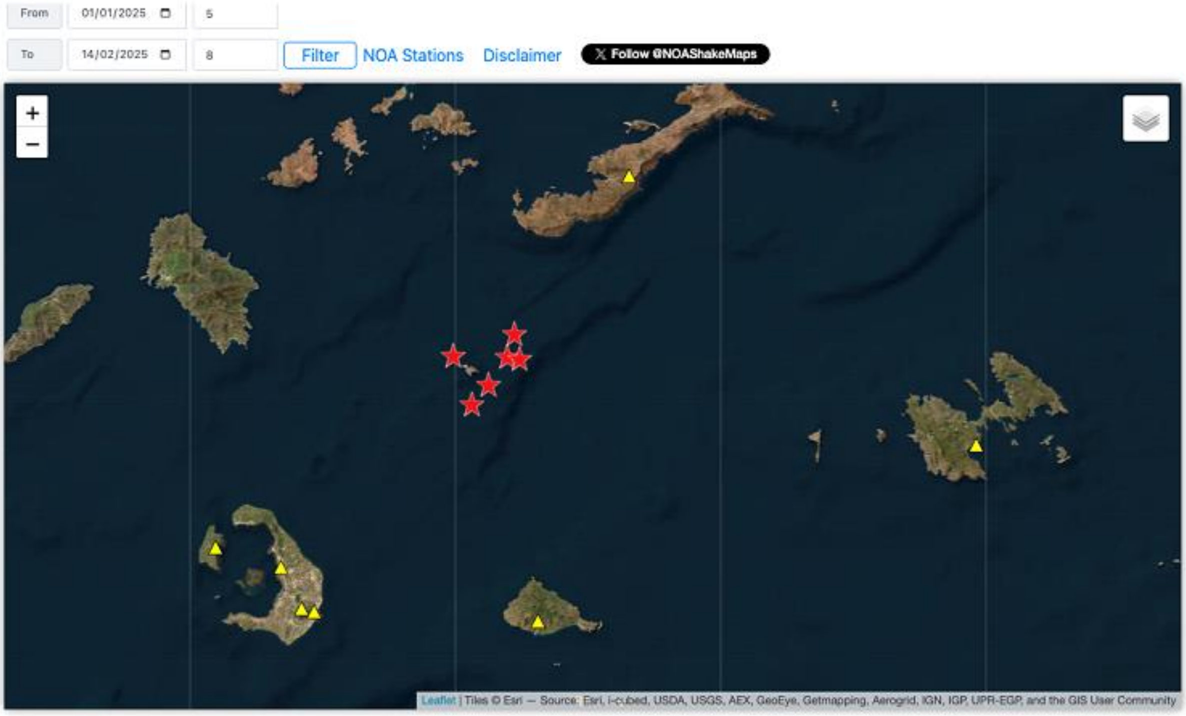

From 01/01/2025 5

To 14/02/2025 8

Figure 10: Selection of earthquakes with magnitude greater than M≥5.0, based on the analysis of the NOAIG, as shown on the website presenting the results of the automatic processing of accelerograms using the USGS ShakeMap software.

Table 1: Data resulting from the automatic analysis of the 7 earthquakes with magnitude M≥5.0

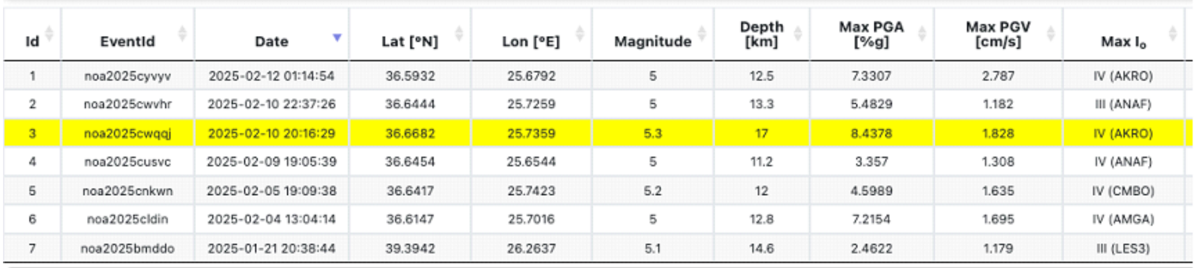

Id	EventId	Date	Lat [°N]	Lon [°E]	Magnitude	Depth [km]	Max PGA [%g]	Max PGV [cm/s]	Max I_o
1	noa2025cyvyv	2025-02-12 01:14:54	36.5932	25.6792	5	12.5	7.3307	2.787	IV (AKRO)
2	noa2025cwvhr	2025-02-10 22:37:26	36.6444	25.7259	5	13.3	5.4829	1.182	III (ANAF)
3	noa2025cwqqj	2025-02-10 20:16:29	36.6682	25.7359	5.3	17	8.4378	1.828	IV (AKRO)
4	noa2025cusvc	2025-02-09 19:05:39	36.6454	25.6544	5	11.2	3.357	1.308	IV (ANAF)
5	noa2025cnkwn	2025-02-05 19:09:38	36.6417	25.7423	5.2	12	4.5989	1.635	IV (CMBO)
6	noa2025cldin	2025-02-04 13:04:14	36.6147	25.7016	5	12.8	7.2154	1.695	IV (AMGA)
7	noa2025bmddo	2025-01-21 20:38:44	39.3942	26.2637	5.1	14.6	2.4622	1.179	III (LES3)

The largest earthquake on 10-02-25 with M=5.3 is shown on the table. For all earthquakes with M≥5, the intensities did not exceed the value of MMI=IV based on instrumental measurements at the locations of the aforementioned stations.

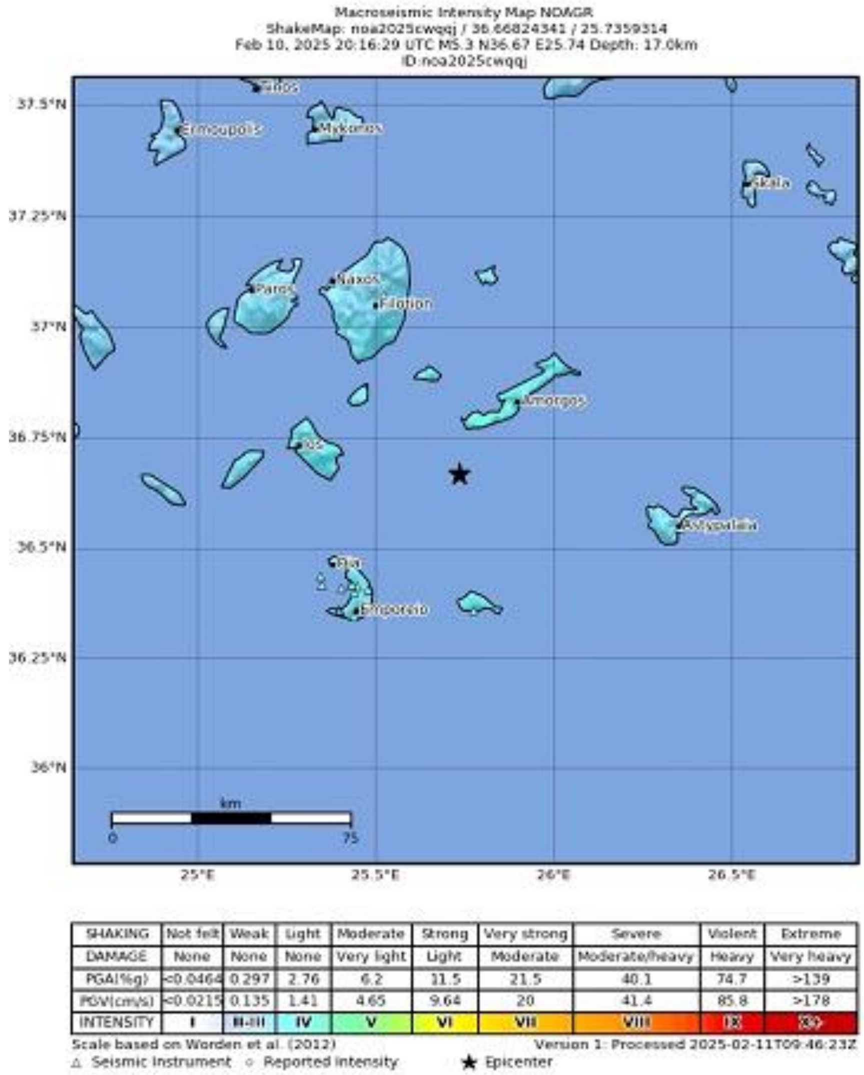

SHAKING	Not felt	Weak	Light	Moderate	Strong	Very strong	Severe	Violent	Extreme
DAMAGE	None	None	None	Very light	Light	Moderate	Moderate/heavy	Heavy	Very heavy
PGA(%g)	<0.0464	0.297	2.76	6.2	11.5	21.5	40.1	74.7	>139
PGV(cm/s)	<0.0215	0.135	1.41	4.65	9.64	20	41.4	85.8	>178
INTENSITY	I	II-III	IV	V	VI	VII	VIII	IX	X+

Scale based on Worden et al. (2012)
Version 1: Processed 2025-02-11T09:46:23Z

△ Seismic Instrument ○ Reported Intensity ★ Epicenter

Figure 11: Shakemap of the largest earthquake using the results of the automatically processed accelerograms and the revised hypocenter and magnitude solutions by the analysis team of NOAIG.

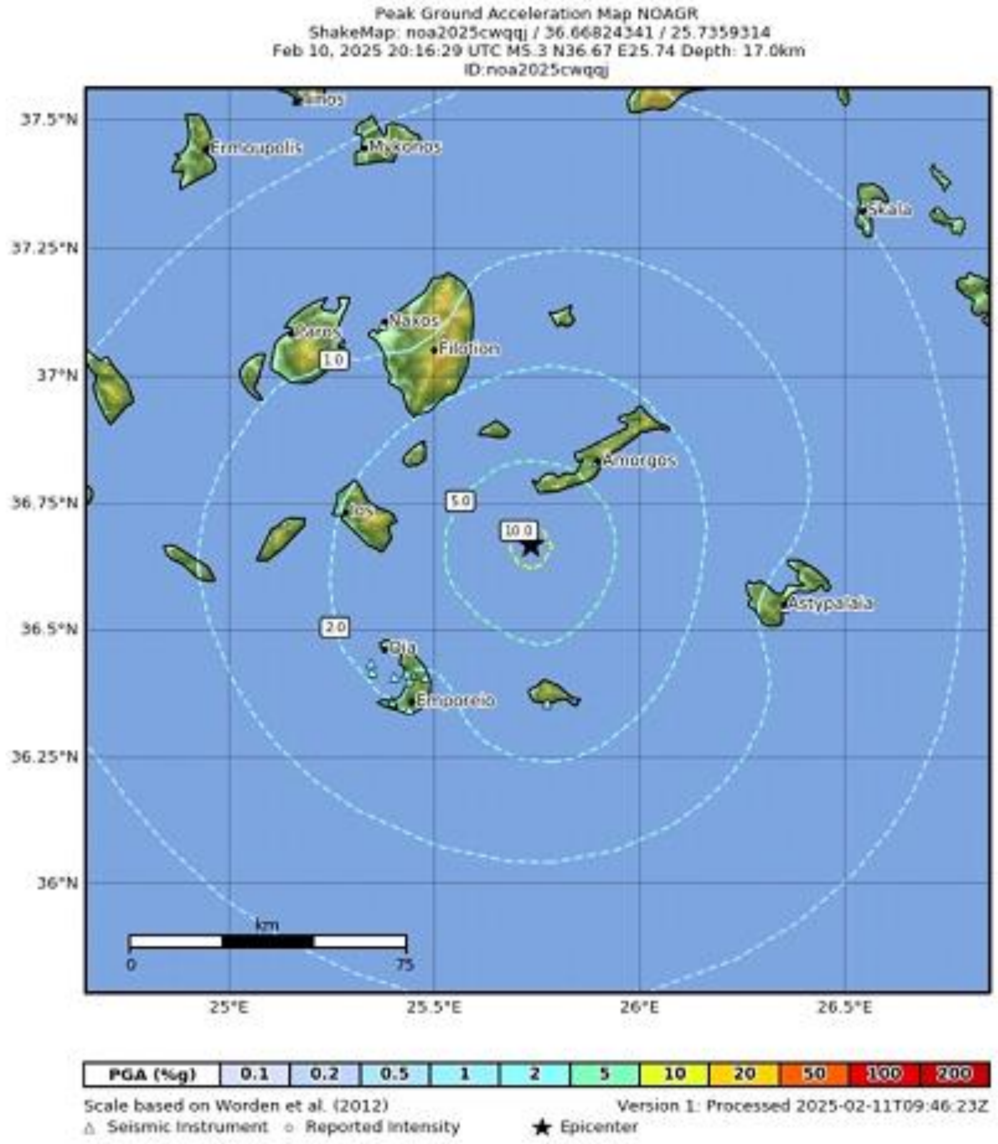

Figure 12: Distribution of the Peak Ground Acceleration of the largest earthquake using the results of the automatically processed accelerograms and the revised hypocenter and magnitude solutions by the analysis team of NOAIG.

Calculation of an optimal 1D velocity model and hypocentral relocation

Figure 13 presents the inversion results of the calculation of the optimal P- and S- velocity models using the VELEST software (Kissling et al. 1995). During the inversion process, 200 initial models (gray color) were used, which were obtained after applying random perturbations to the model proposed by Brüstle et al. (2012) for the region. For the application of the algorithm, only seismic events recorded by all stations close to the sequence (ANYD, ANAF, AMGA, at least 3 stations from Santorini) with an azimuthal gap (GAP) less than 180° were used. Their number amounts to more than 1500 (up to 06/03/2025 23:59). The final models that resulted are shown in red and the optimal final model in black. The graphs also show the number of seismic events versus depth, from which it becomes apparent that the model is reliable for depths up to 12 km. The map in **Figure 14** shows the locations of the relocated epicenters of the total seismicity recorded by the network in the area.

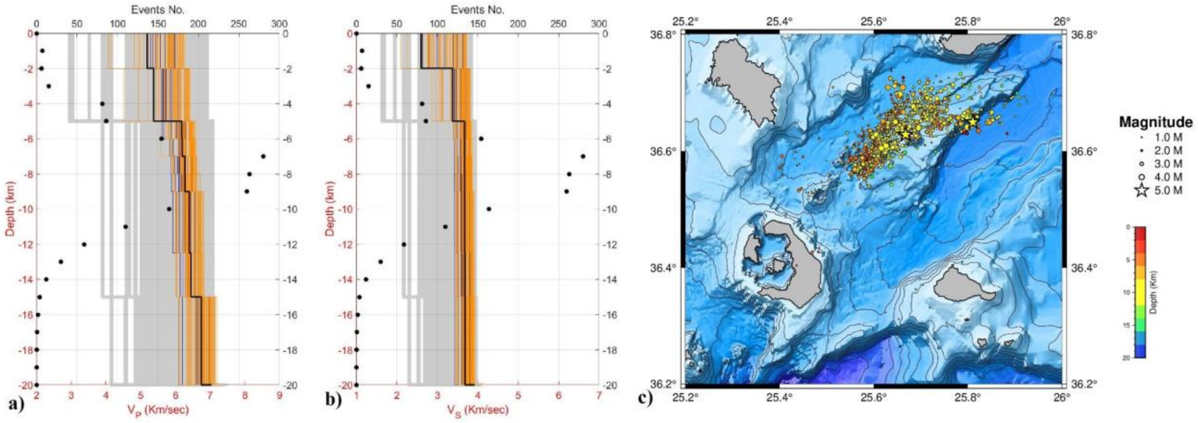

Figure 13: a) Results of the application of the Velest software for P- and **b)** S- velocity models and **c)** the epicentral distribution that resulted after the hypocentral relocation process, for the seismic events that were selected during the inversion process.

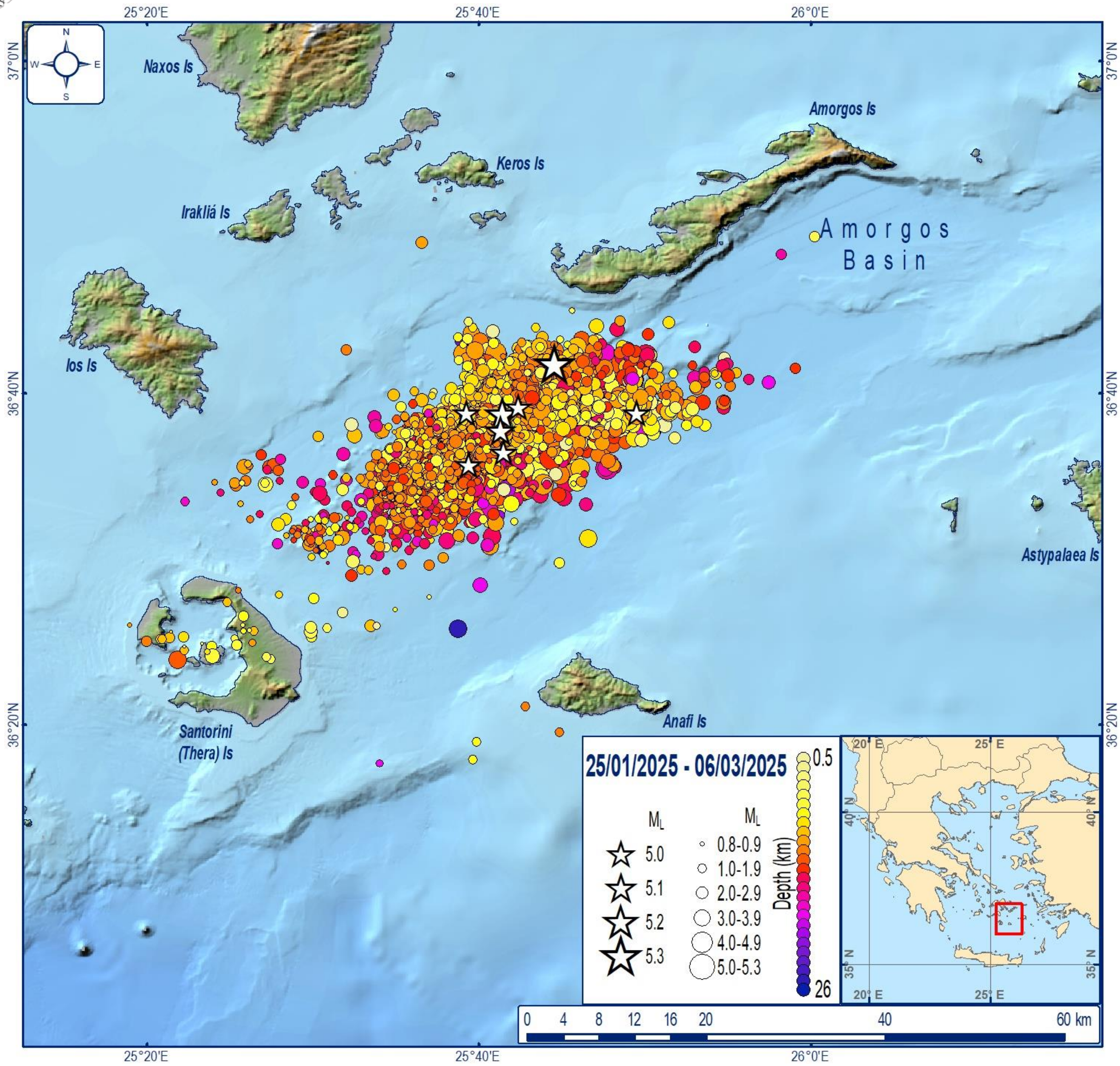

Figure 14: Spatial distribution of epicenters resulting from the hypocentral relocation process for all recorded seismic events.

Full moment tensor inversion based on first motion P-wave polarities

Constrained double couple moment tensors that are routinely calculated by the NOAIG (**Figure 6**, Triantafylis et al., 2022), are usually characterised by a high CLVD component. This may be an indication of errors projected in the moment tensors as a result of high uncertainties in the velocity model and/or high levels of noise in the waveform data. Another possible reason may be the effect of a true non-double-couple source mechanism possibly associated with volume change in the seismic source, as a result of dyke propagation through crustal rocks, given the geological setting between Santorini and Amorgos islands.

In order to investigate this assumption, we apply full moment tensor inversion (Pugh et al. 2016) using an alternative dataset, namely, manually picked first motion P-wave polarities by taking into account a-priori uncertainties based on their observations. Station azimuths and take-off angles are calculated with respect to the reviewed hypocentre locations and a local velocity model (**Figure 13**). We first apply a constrained double-couple inversion, followed by a full moment tensor inversion and we calculate their posterior model probabilities.

Figure 14a shows the beachball of the full moment tensor for the high-CLVD example event (as resulted by Gisola software) of the February 5, 2025, 17:47:26.74 (GMT), M_L 4.7 earthquake. The earthquake mechanism is represented mainly by a double-couple, normal faulting seismic source (80%), 19% isotropic component and just 1% CLVD (**Figure 14c**), whereas, **Figure 14b** highlights the acceptable best-fitting double-couple fault parameters of the full moment tensor. The possible moment tensor component tradeoffs are shown in **Figure 15**, where Mxy-Myz components show a strong linear tradeoff, possibly due to the geometrical strike - slip tradeoff. Finally, the moment tensor decomposition for each model during the full moment tensor inversion is shown in **Figure 16** with the optimal model showing a relatively small isotropic component (19%).

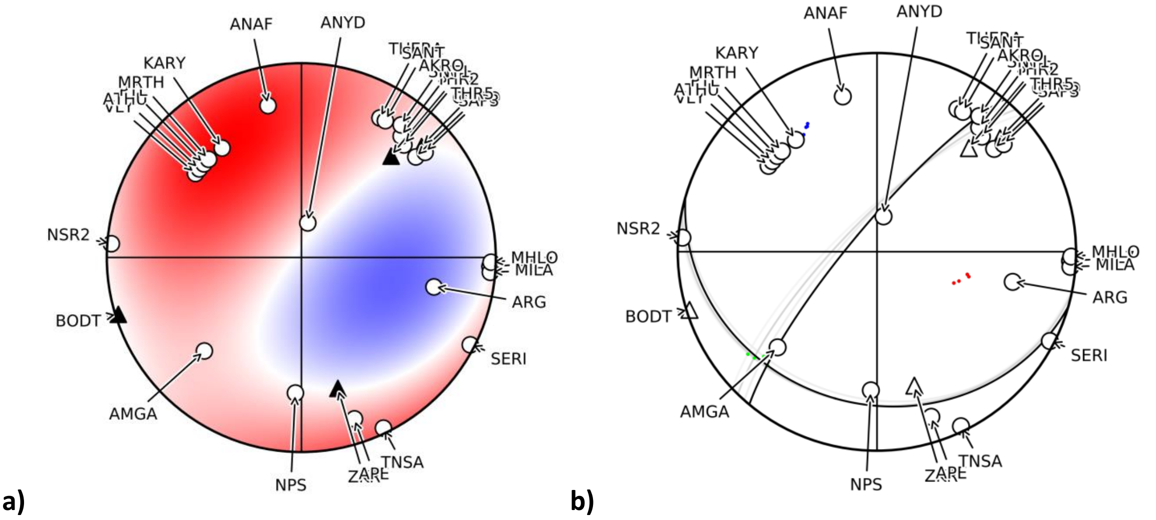

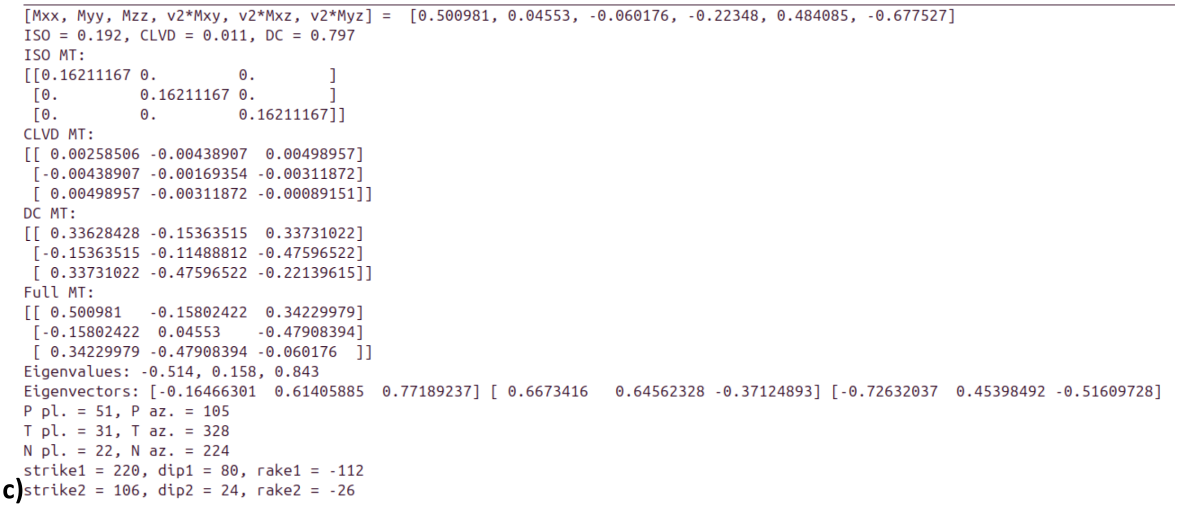

```
[Mxx, Myy, Mzz, v2*Mxy, v2*Mxz, v2*Myz] =  [0.500981, 0.04553, -0.060176, -0.22348, 0.484085, -0.677527]
ISO = 0.192, CLVD = 0.011, DC = 0.797
ISO MT:
[[0.16211167 0.         0.        ]
 [0.         0.16211167 0.        ]
 [0.         0.         0.16211167]]
CLVD MT:
[[ 0.00258506 -0.00438907  0.00498957]
 [-0.00438907 -0.00169354 -0.00311872]
 [ 0.00498957 -0.00311872 -0.00089151]]
DC MT:
[[ 0.33628428 -0.15363515  0.33731022]
 [-0.15363515 -0.11488812 -0.47596522]
 [ 0.33731022 -0.47596522 -0.22139615]]
Full MT:
[[ 0.500981   -0.15802422  0.34229979]
 [-0.15802422  0.04553    -0.47908394]
 [ 0.34229979 -0.47908394 -0.060176  ]]
Eigenvalues: -0.514, 0.158, 0.843
Eigenvectors: [-0.16466301  0.61405885  0.77189237] [ 0.6673416   0.64562328 -0.37124893] [-0.72632037  0.45398492 -0.51609728]
P pl. = 51, P az. = 105
T pl. = 31, T az. = 328
N pl. = 22, N az. = 224
strike1 = 220, dip1 = 80, rake1 = -112
strike2 = 106, dip2 = 24, rake2 = -26
```

c)

Figure 14: **a)** Beachball showing the full moment tensor for the 5 February 2025, 17:47:26.74 (GMT), M_L 4.7 earthquake, using first motion P-wave polarities. White circles represent compressions and black triangles denote dilatations. Red and blue coloured areas represent areas of compression and dilatation, respectively. **b)** Best-fitting double-couple mechanisms based on the full moment tensor for the 5 February 2025, 17:47:26.74 (GMT), M_L 4.7 earthquake. Circles represent compressions and triangles denote dilatations. Red dots represent P principal axes for each model, blue dotes denote the T axes and green dots show the Null axes. In both cases, station codes are shown around the Schmidt net. **c)** Full moment tensor decomposition for the 5 February 2025, 17:47:26.74 (GMT), M_L 4.7 earthquake.

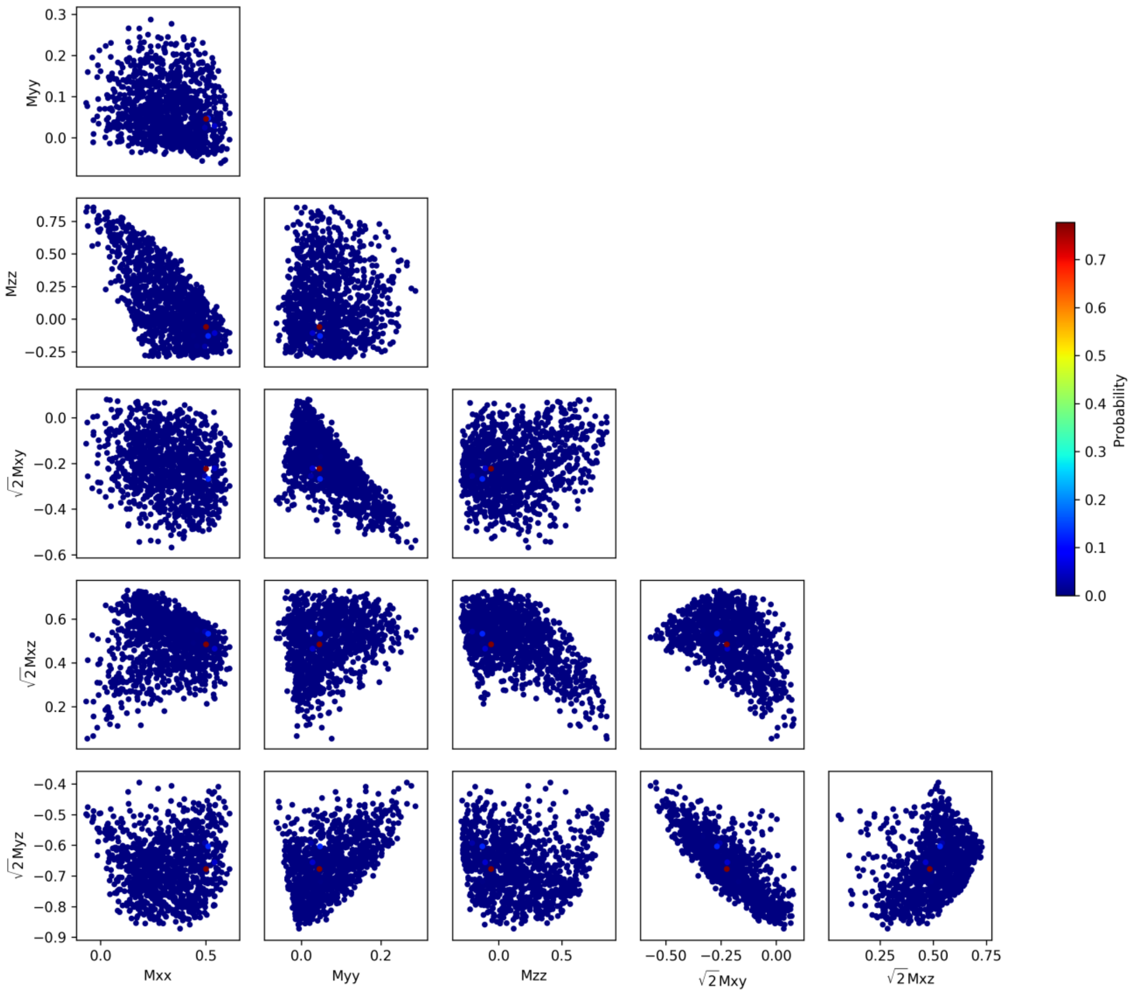

Figure 15: Scatter plots of moment tensor components for the 5 February 2025, 17:47:26.74 (GMT), M_L 4.7 earthquake. The colour scale shows the posterior probability for each model during the full moment tensor inversion.

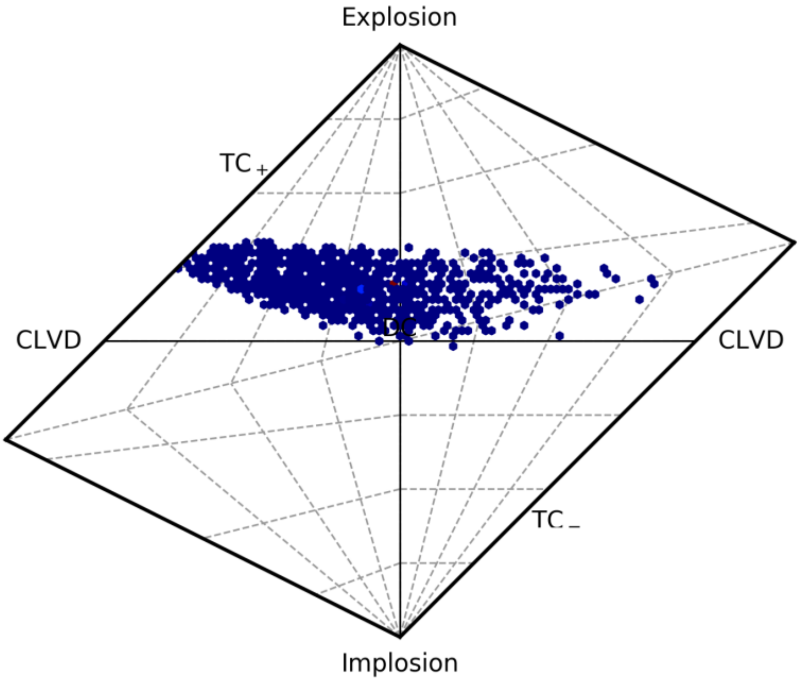

Figure 16: Hudson plot showing the full moment tensor decomposition for each model during the inversion of the 5 February 2025, 17:47:26.74 (GMT), M_L 4.7 earthquake mechanism (see also colour scale in **Figure 15**)

Earthquake catalogue update by applying machine learning methodologies

The seismicity catalog was complemented with small-magnitude earthquakes by applying machine learning algorithms to the waveforms recorded by the network. More specifically, the EQTransformer method (Mousavi et. al, 2020) was applied with the VOLPICK (Volcano Tectonic and Long-Period Earthquakes) and STEAD (STanford EArthquake Dataset) training data, from which a total of ~40000 seismic events were obtained for the period between 01/06/2024 and 05/03/2025. It should be emphasized that the results were evaluated in order to eliminate any erroneous recordings. **Figure 17** presents the events characterized by small location errors, so as to highlight the sequence. This number amounts to 30190 earthquakes. The events were located using the NonLinLoc algorithm (Lomax et al., 2000, 2014) and further refined with the Source-Specific Station Term (Richards-Dinger and Shearer, 2000) method. The local magnitude was determined following Skordilis et al. (2016).

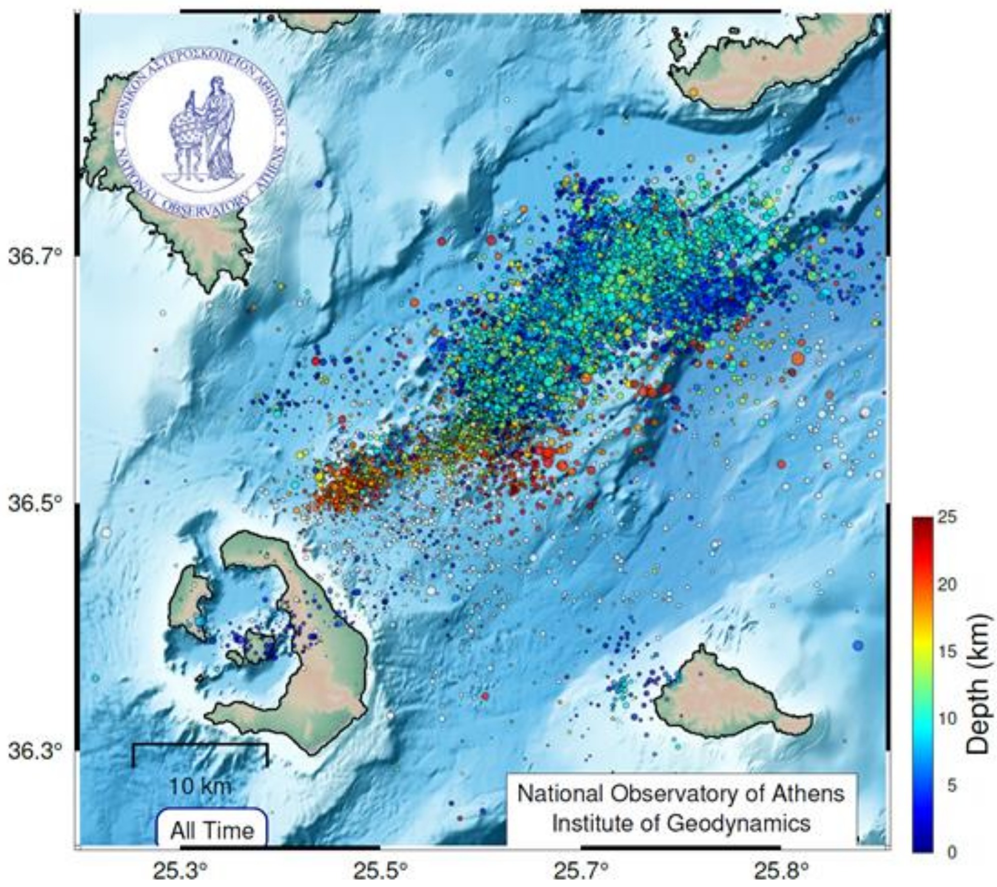

Figure 17: Seismic events that resulted from the application of the EQTransformer algorithm for the period between 1/06/2024 and 05/03/2025 and are characterized by small location errors.

Monitoring deformations in the Santorini area using GNSS data

Regarding the deformation in the Santorini area, the estimation of the daily coordinates of three continuous recording GNSS stations (Imerovigli, Exo Gonia and Perissa) versus time, revealed changes in their movement speeds which began in August 2024 and continue up to this day. These changes, although significant from the beginning, started smoothly but accelerated towards the end of January 2025, particularly for the Imerovigli station. Regarding the vertical plane, all three stations showed an uplift after the start of the change in their kinematic behavior. Regarding the horizontal plane and in the E-W direction, all three stations are moving towards the east, while in the N-S direction, the station in Imerovigli is moving towards the north and the others towards the south. All ground velocity changes that began in August 2024 and were mentioned above are more intense at the Imerovigli station compared to the other two.

Monitoring deformations in the Santorini Caldera for the period 2023-2025 using InSAR data

The geodetic data provided by the Sentinel-1 European Space Agency (ESA) satellite were used in order to determine the location and characteristics of the source of the deformation around the Santorini volcano, either a Mogi-source type of source as the 2011-2012 episode (Parks et al. 2012) or a propagating dyke. Our InSAR analysis covers the period from October 2023 to January 2025 and leverages LiCSBAS, an open-source package (Morishita et al., 2020), for InSAR time series analysis with the N-SBAS method. We used LiCSAR generated interferograms, both wrapped and unwrapped, from Sentinel-1 SLC (Single Look Complex) data and implemented the data analysis procedures as described in Tsironi et al. (2024). Phase coherence exceeded the value of 0.5 in most areas. The results of the InSAR analysis indicate uplift rates of up to +35 mm/year (**figure 18**) that are more supportive of a Mogi-type model for the area within the caldera. The highest values occur around the northern part of the caldera, in Thirasia, Fira, Oia and the northern part of the islet of Nea Kammeni.

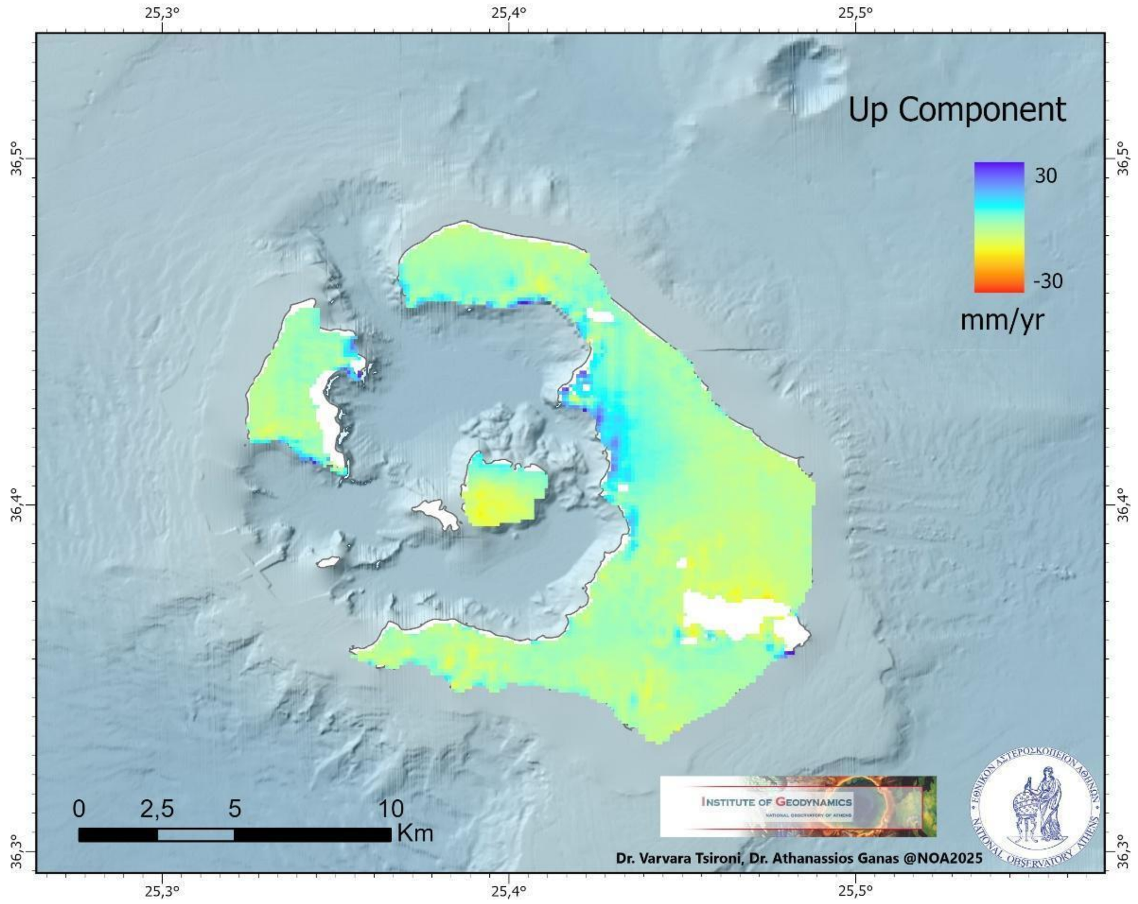

Figure 18: Map showing the ground velocities distribution for the vertical component. Areas with uplift are shown in cyan & blue (positive values). The highest velocities are found in the Oia area, Fira, Thirasia and northern Nea Kammeni with values up to 3.5 cm per year.

Processing of strong motion recordings

Recordings of earthquakes with magnitude M_L3.9 and above were collected from both broadband and strong-motion sensors and processed according to PEER strong-ground motion analysis standards (Kishida et al., 2016; Ktenidou et al., 2024). The analysis was limited to data from selected stations with epicentral distances up to 140 km. **Figure 19** shows the stations studied and their relative location to the seismic sequence (top) as well as the magnitude-distance distribution (bottom).

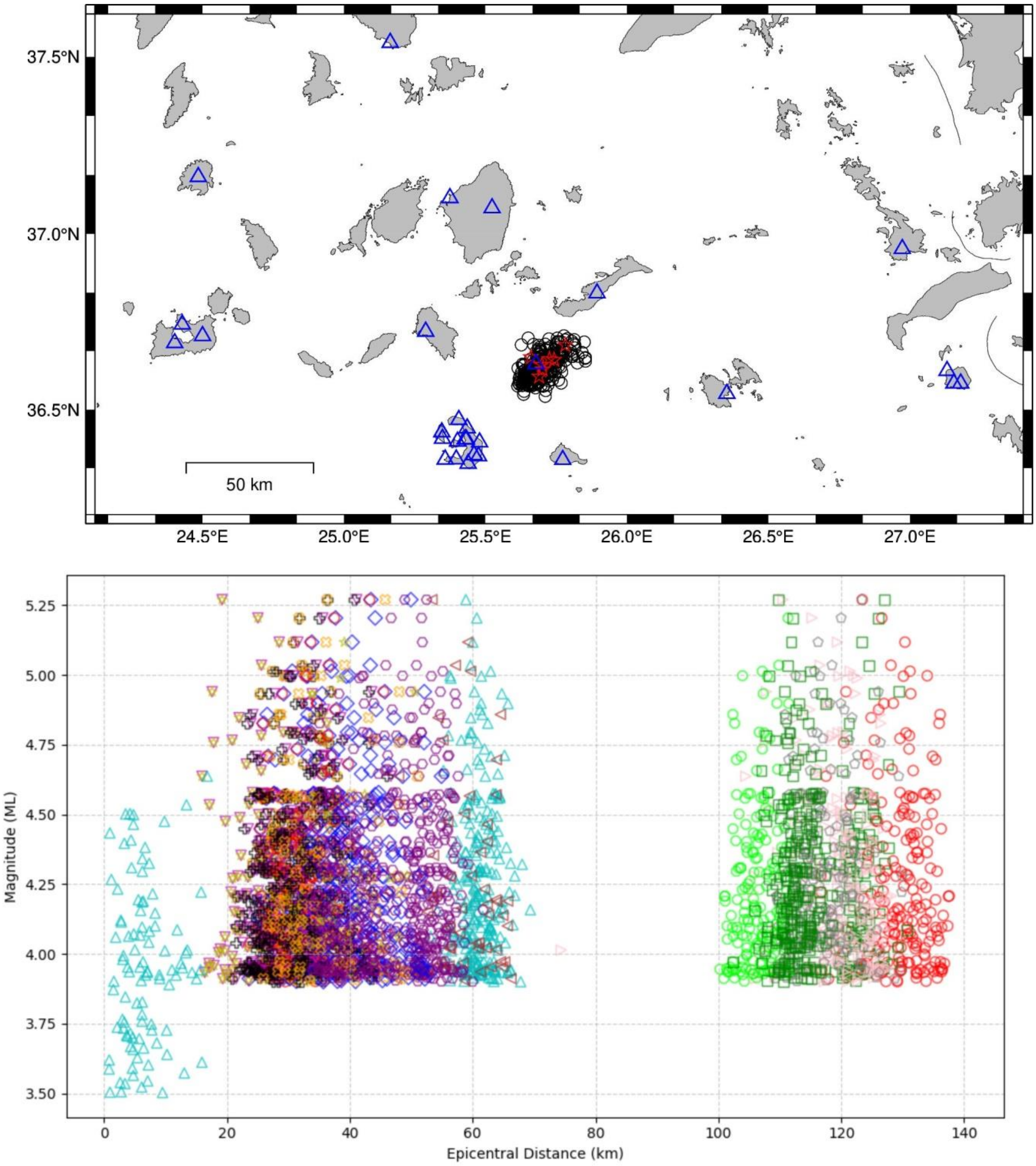

Figure 19: Top: Map showing station locations and indicative epicentral locations for events larger than M3.9 (HT.ANYD). Bottom: Magnitude-distance distribution of the data already analyzed for the period 01-17/02/2025, colour-coded by station.

More than 4,500 recordings were deemed to be of acceptable quality for the period from 1/2 to 17/2, while a great number of recordings in the initial dataset were rejected due to low quality, primarily because of high noise level. Quality control is an important step in this case, due to the very high likelihood of contamination of the signal under study by smaller earthquakes that occur very frequently (e.g. **figure 20** illustrates an example of a 200-second time series with at least 6 events).

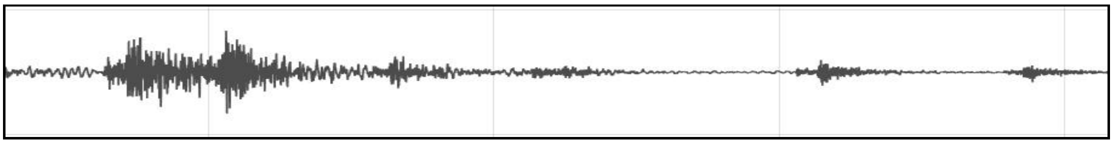

Figure 20: Example of a 200 sec time series indicative of the noise level in several of the recordings of the sequence

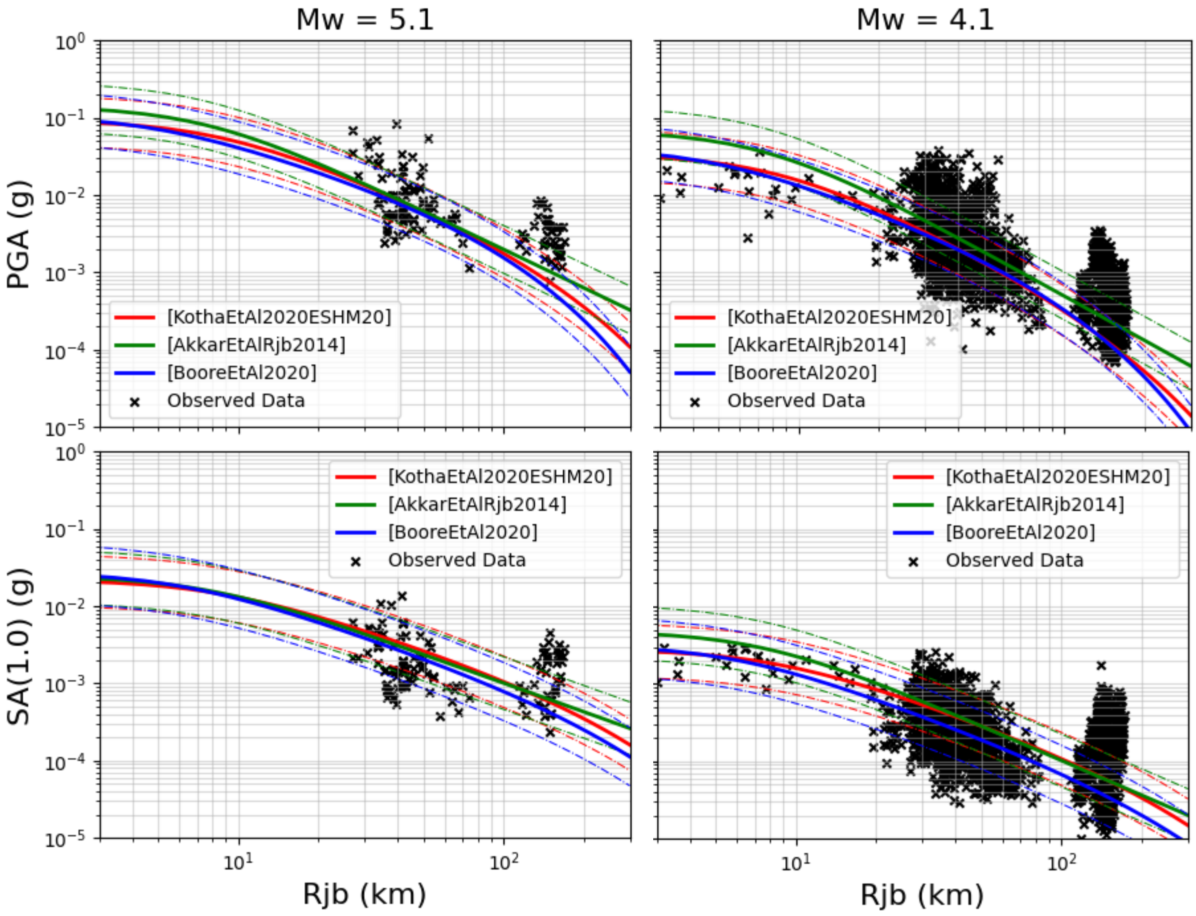

Figure 21: Comparison of observed peak ground acceleration (PGA-top) and spectral acceleration at T=1 s (bottom) across all the stations studied with 3 attenuation relationships for shallow tectonic earthquakes. Comparisons are shown for earthquakes within a magnitude bin of M_W5.0-5.2 (left) and M_W4.0-4.2 (right).

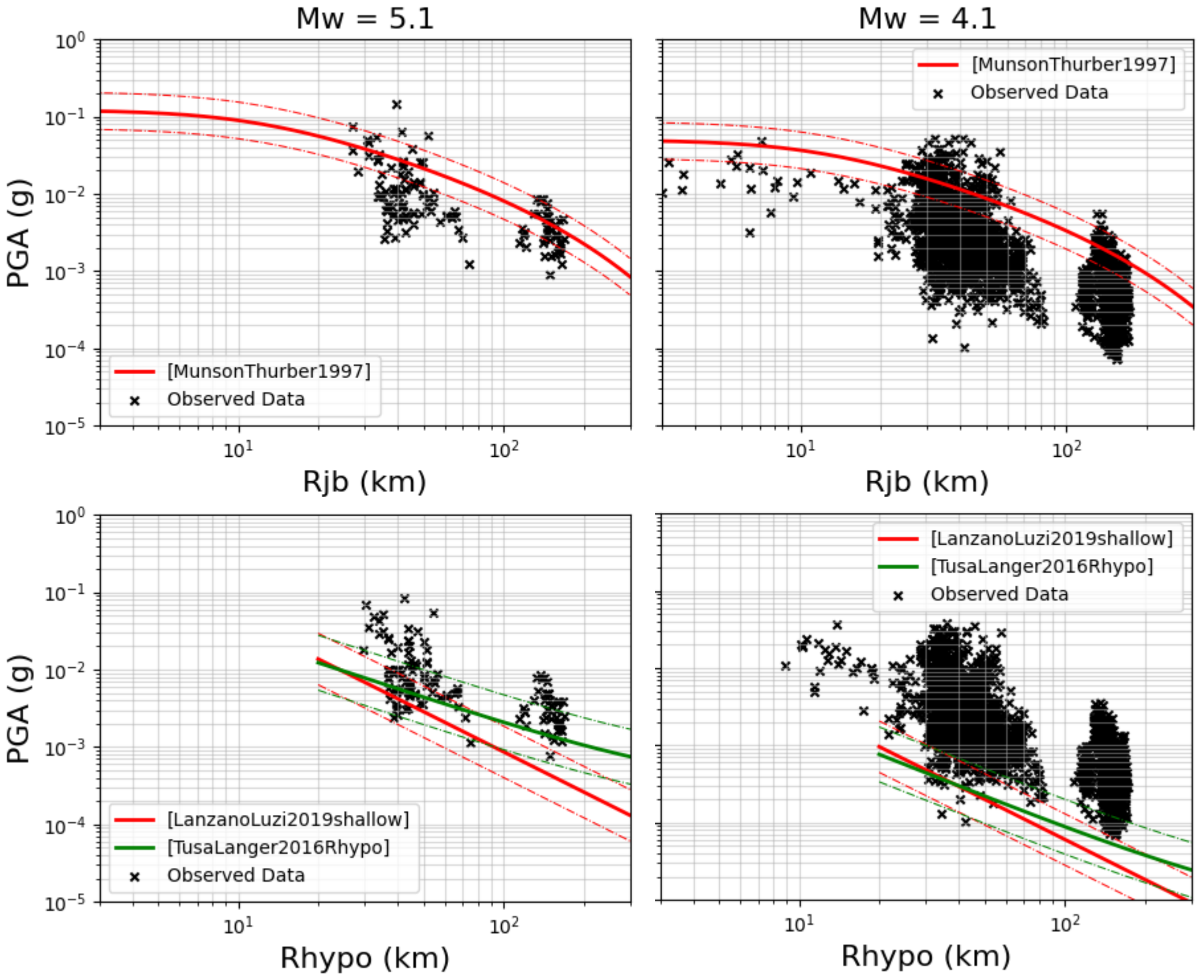

Figure 22: Comparison of observed peak ground acceleration (PGA) values across all stations studied with attenuation relationships for volcanic ground motions in Hawaii (top) and Italy (bottom). Comparisons are shown for earthquakes within a magnitude bin of M_W5.0-5.2 (left) and M_W4.0-4.2 (right).

Following the quality control and processing of the data, response spectra were calculated and a preliminary comparison was made with some reference ground motion models (GMMs) for shallow tectonic earthquakes in Europe (Akkar and Bommer, 2014; Boore et al., 2020; Kotha et al., 2020). **Figure 21** compares the observed peak ground acceleration (PGA) and 1-sec spectral acceleration values at the stations under study with these tectonic shallow crustal model predictions within one standard deviation from the mean estimate (solid and dashed lines). This is shown as a function of distance for rock site conditions (800 m/s) for two magnitude bins, M_W5.0-5.2 (left) and M_W4.0-4.2 (right), the latter case allowing inspection of data for the near-source station HT.ANYD. **Figure 22** makes a comparison between observations and three volcanic earthquake GMMs that were calibrated for Italy (Lanzano and Luzi, 2019; Tusa and Langer, 2016) and Hawaii (Munson and Thurber, 1997).

No accelerations values greater than 0.33g (3.3 m/s^2, see **figure 21**) were observed. Only a few PGA values were observed above 0.1g, which is consistent with the absence of observed damage on the nearby islands. However, there is significant scatter in the recorded values for similar M-R scenarios, which may be related to the conditions at the individual stations, the azimuth, the path, the source characteristics and type, etc. Due to the PGA values and the generally rocky conditions, no significant nonlinearity is expected.

Institute of Geodynamics – National Observatory of Athens

https://www.gein.noa.gr/

The following Researchers, Scientists, Technicians and Scientific Associates worked within the framework of the above work, carried out by the Institute of Geodynamics of the National Observatory of Athens:

The list is in alphabetical order:

Athanasopoulou, M., Boukouras, K., Charalampakis, M., Chousianitis, K., Cekinmez, Z., Daskalaki, E., Doukas, L., Evangelidis, C., Fountoulakis, I., Fragouli, K., Ganas, A., Gkika, F., Halaris, F., Kalligeris, N., Karastathis, V., Kontakos, K., Ktenidou, O. J., Lantzourakis, P., Lentas, K., Liadopoulos, E., Liakopoulos, S., Makaris, D., Melis, N., Michas, G., Mouzakiotis, E., Mouslopoulou, V., Novikova, T., Panopoulou, G., Papageorgiou, A., Pikoulis, E. V., Polimenakos, S., Poulimenos, S., Rigopoulos, A., Sachpazi, M., Samios, M., Sboras, S., Tsironi, V., Tzortzopoulou, M., Venizelos, D., Vogiannis, E.

References

Andinisari, R., Konstantinou, K. I., & Ranjan, P. (2021). Seismicity along the Santorini-Amorgos zone and its relationship with active tectonics and fluid distribution. P*hysics of the Earth and Planetary Interiors*, **312**, 106660.

Akkar S, Sandikkaya MA, Bommer JJ (2014) Empirical ground-motion models for point- and extended source crustal earthquake scenarios in Europe and the Middle East. *Bull Earthq Eng* **12**:359–387

Boore, D. M., J. P. Stewart, A. A. Skarlatoudis, E. Seyhan, B. Margaris, N. Theodoulidis, E. Scordilis, I. Kalogeras, N. Klimis, and N. S. Melis (2020). A Ground-Motion Prediction Model for Shallow Crustal Earthquakes in Greece, *Bull. Seismol. Soc. Am*. **111**, 857–874.

Brüstle, A., Kueperkoch, L., Rische, M., Meier, T., Friederich, W., & Egelados Working Group. (2012, April). Seismicity of the eastern Hellenic subduction zone. In *EGU General Assembly Conference Abstracts* (p. 10426).

Kanamori, H., & Heaton, T. H. (2000). Microscopic and macroscopic physics of earthquakes. *Geocomplexity and the Physics of Earthquakes*, **120**, 147-163.

Kishida, T., Ktenidou, O-J., Darragh, R. and Silva, W. (2016): Semi-automated procedure for windowing time series and computing Fourier Amplitude Spectra (FAS) for the NGA-west2 database. PEER report 2016/02, Berkeley, CA: Pacific Earthquake Engineering Research Center, 63.

Kissling, E., Kradolfer, U., & Maurer, H. (1995). Program VELEST user's guide-Short Introduction. *Institute of Geophysics, ETH Zurich*, *22*.

Kotha, S. R., Weatherill, G., Bindi, D., & Cotton, F. (2020). A regionally-adaptable ground-motion model for shallow crustal earthquakes in Europe. *Bulletin of Earthquake Engineering*, **18**(9), 4091-4125.

Ktenidou, O. J., Papageorgiou, A., Pikoulis, E. V., Liakopoulos, S., Gkika, F., Cekinmez, Z., ... & Evangelidis, C. P. (2024). The quest for reference stations at the National Observatory of Athens, Greece. *Natural Hazards and Earth System Sciences Discussions*, 2024, 1-29.

Lanzano, G., & Luzi, L. (2020). A ground motion model for volcanic areas in Italy. *Bulletin of earthquake engineering*, **18**(1), 57-76.

Lomax, A., Virieux, J., Volant, P., and Berge-Thierry, C. Probabilistic Earthquake Location in 3D and Layered Models, pages 101–134. Springer Netherlands, 2000. doi: 10.1007/978-94-015-9536-05.88

Lomax, A., Michelini, A., and Curtis, A. Earthquake Location, Direct, Global-Search Methods, pages 1–33. Springer New York, New York, NY, 2014. doi: 10.1007/978-3-642-27737-5150 − 2.

Morishita, Y., Lazecky, M., Wright, T.J., Weiss, J.R., Elliott, J.R., Hooper, A. (2020). LiCSBAS: An Open-Source InSAR Time Series Analysis Package Integrated with the LiCSAR Automated Sentinel-1 InSAR *Processor. Remote Sens*., **12**, 424

Mousavi, S. M., Ellsworth, W. L., Zhu, W., Chuang, L. Y., & Beroza, G. C. (2020). Earthquake transformer—an attentive deep-learning model for simultaneous earthquake detection and phase picking. *Nature communications*, **11**(1), 3952.

Munson, C. G., & Thurber, C. H. (1997). Analysis of the attenuation of strong ground motion on the island of Hawaii. *Bulletin of the Seismological Society of America*, *87*(4), 945-960.

Nomikou, P., Hübscher, C., Papanikolaou, D., Farangitakis, G. P., Ruhnau, M., & Lampridou, D. (2018). Expanding extension, subsidence and lateral segmentation within the Santorini-Amorgos basins during Quaternary: Implications for the 1956 Amorgos events, central-south Aegean Sea, Greece. *Tectonophysics*, **722**, 138-153.

Parks, M. M., Biggs, J., England, P., Mather, T. A., Nomikou, P., Palamartchouk, K., ... & Zacharis, V. (2012). Evolution of Santorini Volcano dominated by episodic and rapid fluxes of melt from depth. *Nature Geoscience*, **5**(10), 749-754.

Pugh, D. J., White, R. S., & Christie, P. A. F. (2016). A Bayesian method for microseismic source inversion. *Geophysical Journal International*, **206**(2), 1009-1038.

Richards-Dinger, K. B. and Shearer, P. M. Earthquake locations in southern California obtained using source-specific station terms. *Journal of Geophysical Research: Solid Earth,* **105**(B5):10939–10960, 2000. doi: https://doi.org/10.1029/2000JB900014.

Scordilis, E. M., Kementzetzidou, D., and Papazachos, B. C. Local magnitude calibration of the Hellenic Unified Seismic Network. *Journal of Seismology*, **20**(1):319–332, 2016. doi: 10.1007/s10950-015-9529-5.

Triantafyllis, N., Venetis, I. E., Fountoulakis, I., Pikoulis, E. V., Sokos, E., & Evangelidis, C. P. (2022). Gisola: A high-performance computing application for real-time moment tensor inversion. *Seismological Society of America*, **93**(2A), 957-966.

Tsironi, V., Ganas, A., Valkaniotis, S., Kouskouna, V., Sokos, E., Koukouvelas, I. (2024). Active shortening and aseismic slip along the Cephalonia Plate Boundary (Paliki Peninsula, Greece): Evidence from InSAR and GNSS data. *Tectonophysics*, v. **884**, 230400, https://doi.org/10.1016/j.tecto.2024.230400.

Tusa, G., & Langer, H. (2016). Prediction of ground motion parameters for the volcanic area of Mount Etna. *Journal of Seismology*, *20*, 1-42.